

# Accelerated Diffusion Weighted Magnetic Resonance Imaging at 7 T: Joint Reconstruction for Shift-Encoded Navigator-based Interleaved Echo Planar Imaging (JETS-NAViEPI)

Zhengguo Tan<sup>a,d</sup>, Patrick Alexander Liebig<sup>b</sup>, Robin Martin Heidemann<sup>b</sup>,  
Frederik Bernd Laun<sup>c</sup>, Florian Knoll<sup>a</sup>

<sup>a</sup>*Department Artificial Intelligence in Biomedical Engineering (AIBE),  
Friedrich-Alexander University of Erlangen-Nuremberg, Erlangen, Germany*

<sup>b</sup>*Siemens Healthcare GmbH, Erlangen, Germany*

<sup>c</sup>*Institute of Radiology, University Hospital Erlangen, Friedrich-Alexander University of  
Erlangen-Nuremberg, Erlangen, Germany*

<sup>d</sup>*Corresponding author: zhengguo.tan@gmail.com*

---

## Abstract

The pursuit of high spatial-angular-temporal resolution for in vivo diffusion-weighted magnetic resonance imaging (DW-MRI) at ultra-high field strength (7 T and above) is important in understanding brain microstructure and function. Such pursuit, however, faces several technical challenges. First, increased off-resonance and shorter  $T_2$  relaxation require faster echo train readouts. Second, existing high-resolution DW-MRI techniques usually employ in-plane fully-sampled multi-shot EPI, which not only prolongs the scan time but also induces a high specific absorption rate (SAR) at 7 T. To address these challenges, we develop in this work navigator-based interleaved EPI (NAViEPI) which enforces the same effective echo spacing (ESP) between the imaging and the navigator echo. First, NAViEPI renders no distortion mismatch between the two echoes, and thus simplifies shot-to-shot phase

variation correction. Second, NAViEPI allows for a large number of shots (e.g.  $> 4$ ) with undersampled iEPI acquisition, thereby rendering clinically-feasible high-resolution sub-millimeter protocols. To retain signal-to-noise ratio (SNR) and to reduce undersampling artifacts, we developed a  $k_y$ -shift encoding among diffusion encodings to explore complementary  $k$ - $q$ -space sampling. Moreover, we developed a novel joint reconstruction with overlapping locally low-rank regularization generalized to the multi-band multi-shot acquisition at 7 T (dubbed JETS-NAViEPI). Our method was demonstrated with experimental results covering 1 mm isotropic resolution multi  $b$ -value DWI and sub-millimeter in-plane resolution fast TRACE acquisition.

*Keywords:* Diffusion-weighted magnetic resonance imaging, Echo planar imaging, Navigator, Ultra-high field, Joint reconstruction, Low rank

---

<sup>1</sup> **1. Introduction**

<sup>2</sup> Diffusion-weighted magnetic resonance imaging (DW-MRI) ([Le Bihan et al., 1986; Merboldt et al., 1985](#)) is a non-invasive modality that is sensi-  
<sup>3</sup> tive to the intravoxel Brownian motion of water molecules. DW-MRI forms  
<sup>4</sup> the basis for diffusion tensor imaging (DTI) ([Basser et al., 1994; Mori et al., 1999](#)) and high angular resolution diffusion imaging (HARDI) ([Tuch et al., 2002](#)), and has been widely used in acute brain ischemia diagnosis, in tumor  
<sup>5</sup> detection and staging, and in neuroscience ([Jones, 2010](#)).

<sup>6</sup> For DW-MRI acquisition, the commonly used pulse sequence is single-  
<sup>7</sup> shot echo-planar imaging (SS-EPI) ([Mansfield, 1977](#)). SS-EPI is capable of  
<sup>8</sup> rapidly acquiring one DW image per radio-frequency excitation at the order  
<sup>9</sup> of 100 ms, and is thus motion robust. However, conventional SS-EPI, even  
<sup>10</sup> with three-fold accelerated acquisition ([Bammer et al., 2001](#)) using parallel  
<sup>11</sup> imaging ([Roemer et al., 1990; Ra and Rim, 1993; Pruessmann et al., 1999](#);  
<sup>12</sup> [Griswold et al., 2002](#)), still suffers from low spatial resolution and geometric  
<sup>13</sup> distortions.

<sup>14</sup> In the quest for high spatial-angular-temporal-resolution and minimal-  
<sup>15</sup> geometry-distortion DW-MRI, tremendous efforts have been made. Tech-  
<sup>16</sup> niques for the correction of image distortions induced by off-resonances and  
<sup>17</sup> eddy currents have been developed ([Andersson et al., 2003](#)). Furthermore,  
<sup>18</sup> gSlider ([Setsompop et al., 2018](#)) with blipped-CAIPI ([Setsompop et al., 2012](#))  
<sup>19</sup> for simultaneous multi-slice (SMS) ([Maudsley, 1980; Breuer et al., 2005](#))  
<sup>20</sup> was proposed to achieve high-resolution DW-MRI. Advanced pulse sequences  
<sup>21</sup> based on multi-shot EPI have also been developed, including but not limited  
<sup>22</sup> to interleaved EPI (iEPI) ([Butts et al., 1993](#)), PROPELLER ([Pipe et al., 2004](#)),

<sup>26</sup> 2002), and readout-segmented EPI (rsEPI) (Porter and Heidemann, 2009;  
<sup>27</sup> Heidemann et al., 2010).

<sup>28</sup> Based on four-shot iEPI, multiplexed sensitivity encoding (MUSE) image  
<sup>29</sup> reconstruction achieved DW-MRI with a sub-millimeter in-plane resolution  
<sup>30</sup> and maximal  $b$ -value  $800 \text{ s/mm}^2$  at 3 T (Chen et al., 2013). The four-shot  
<sup>31</sup> iEPI employed in MUSE acquired an in-plane fully-sampled  $k$ -space, except  
<sup>32</sup> partial Fourier. Every shot (segment), corresponding to four-fold under-  
<sup>33</sup> sampling, was then reconstructed via parallel imaging to obtain shot-to-shot  
<sup>34</sup> phase variation. This indicates that increasing the number of shots in MUSE  
<sup>35</sup> will result in higher undersampling per shot, and consequently, degrade shot  
<sup>36</sup> phase estimation (Wu and Miller, 2017).

<sup>37</sup> Alternatively, navigator-based iEPI acquisition has been proposed (Jeong  
<sup>38</sup> et al., 2013; Dai et al., 2017, 2018). These proposals allow for a larger num-  
<sup>39</sup> ber of shots, and hence higher spatial resolution. However, due to the use of  
<sup>40</sup> different ESP between the imaging echo and the navigator echo, these pro-  
<sup>41</sup> posals suffered from geometric distortion mismatch between the two echoes  
<sup>42</sup> and thus required specific compensation methods. In contrast, rsEPI (Porter  
<sup>43</sup> and Heidemann, 2009; Heidemann et al., 2010) used the same readout seg-  
<sup>44</sup> ment for both echoes, and thus required no distortion correction of navigator  
<sup>45</sup> echoes.

<sup>46</sup> Beyond the MUSE-type parallel imaging reconstruction, compressed sens-  
<sup>47</sup> ing (Lustig et al., 2007; Block et al., 2007) has been explored. For instance,  
<sup>48</sup> multi-shot reconstruction techniques based on structured low-rank matrix  
<sup>49</sup> completion (MUSSELS) (Mani et al., 2017; Bilgic et al., 2019) achieved 5-  
<sup>50</sup> shot DW-MRI with 9-fold undersampling per shot. Recently, JULEP (Dai

51 et al., 2023) incorporated explicit phase mapping into MUSSELS. These re-  
52 construction techniques, i.e., MUSE, MUSSELS and JULEP, targeted the  
53 reconstruction of one DW image from interleaved EPI acquisition, and did  
54 not explore joint- $k$ - $q$ -space undersampling or reconstruction.

55 Joint- $k$ - $q$ -space undersampling can be achieved via proper regularization  
56 along the diffusion encoding direction. Relevant examples are diffusion un-  
57 dersampling with Gaussian process estimated reconstruction (DAGER) (Wu  
58 et al., 2019) and magnitude-based spatial-angular locally low-rank regular-  
59 ization (SPA-LLR) (Hu et al., 2020). However, DAGER addressed the re-  
60 construction problem of single-shot EPI acquisition and SPA-LLR focused  
61 on the reconstruction of single-band and fully-sampled iEPI acquisition.

62 In this work, we propose a Joint  $k$ - $q$ -slice rEconsTruction framework  
63 for Shift-encoded NAVigator-based interleaved EPI at 7 T (dubbed JETS-  
64 NAViEPI). Our pulse sequence, NAViEPI, differs from most existing tech-  
65 niques. First, NAViEPI builds upon interleaved EPI, thereby allowing for  
66 fast and efficient  $k$ -space coverage. Second, inspired by rsEPI, NAViEPI en-  
67 sures the same effective ESP between the imaging and the navigator echo,  
68 thereby minimizing geometric distortion and allowing for the use of a larger  
69 number of shots. NAViEPI essentially integrates the advantages of both iEPI  
70 and rsEPI. Third, NAViEPI utilizes undersampled multi-shot iEPI, thereby  
71 alleviating the SAR problem at 7 T. Fourth, NAViEPI shifts the  $k$ -space in-  
72 plane sampling pattern along the phase encoding ( $k_y$ ) direction. This shifting  
73 creates complementary  $k$ - $q$ -space sampling, which leads to the possibility of  
74 our joint  $k$ - $q$ -slice reconstruction. Specifically, we employ spatial-diffusion  
75 overlapping LLR regularization to jointly reconstruct all diffusion encodings

<sup>76</sup> and multi-band slices. In vivo experiments at 7 T and comparisons with other  
<sup>77</sup> techniques demonstrate the efficiency of our proposed method in achieving  
<sup>78</sup> high spatial resolution DW-MRI at ultra-high field.

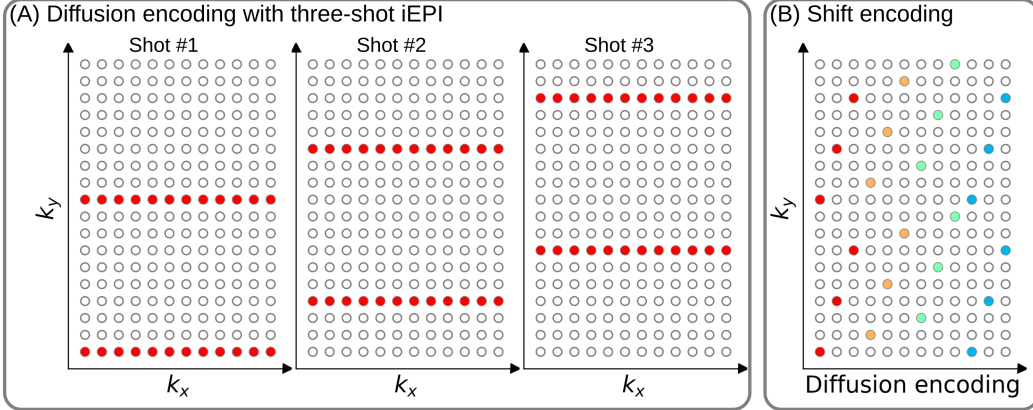


Figure 1: (A) An example DW-MRI acquisition with three-shot interleaved EPI acquisition. (B) The proposed  $k_y$  shifted diffusion encoding scheme. This example employs three shots per DW image. Therefore, every three columns have the same color.

## 79 2. Materials and methods

### 80 2.1. Multi-band shift-encoded iEPI acquisition

81 Fig. 1 (A) displays the diffusion-weighted image acquisition based on  
 82 three-shot interleaved EPI with three-fold in-plane undersampling. Conven-  
 83 tionally, such a sampling pattern is repeated for all diffusion directions. In  
 84 contrast, we propose the  $k_y$ -shifted diffusion encoding, as shown in Fig. 1 (B).  
 85 The interleaved EPI sampling pattern is shifted by one  $k_y$  line per diffusion  
 86 direction, with the cycling period being the in-plane undersampling factor.

87 It is worth noting that, as shown in Fig. 1 (A), the undersampling factor  
 88 of one segment is  $R_{\text{in-plane}} \times N_{\text{shot}}$  (ignore multi-band undersampling here),  
 89 yielding nine-fold in-plane undersampling in this example. In other words,  
 90 the undersampling factor per segment linearly scales up with the number  
 91 of shots. Consequently, conventional self-gating reconstruction techniques,  
 92 e.g. MUSE, suffer from degraded shot-to-shot phase estimation, which in

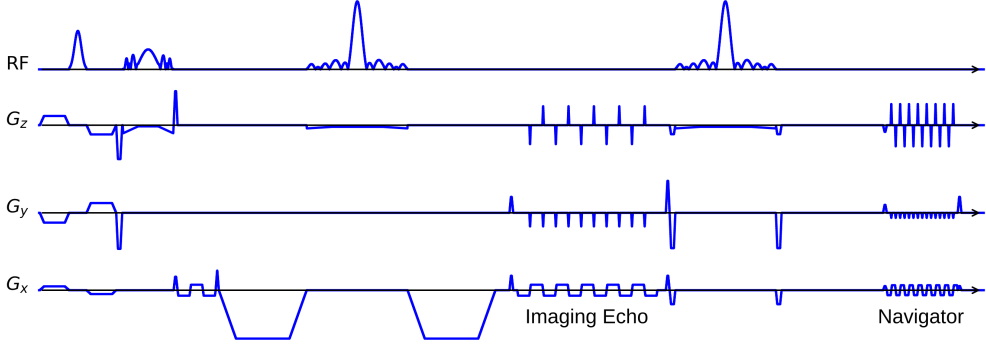


Figure 2: The NAViEPI sequence diagram. SMS is utilized for the acquisition of both imaging and navigator echoes. While the acceleration factor per navigator is the same as listed in Table 1, the acceleration factor per imaging echo is in addition linearly scaled by the number of shots.

93 turn limits the number of shots and spatial resolution.

94 *2.2. NAViEPI: Navigator-based iEPI with consistent effective ESP between  
95 the imaging and the navigator echo - where iEPI meets rsEPI*

96 Instead of the self-gated MUSE with in-plane fully-sampled iEPI and  
97 a limited number of shots, We propose NAVigator-based interleaved EPI  
98 (NAViEPI), as illustrated in Fig. 2. Inspired by rsEPI (Porter and Hei-  
99 demann, 2009), NAViEPI enforces a consistent effective ESP between the  
100 imaging and the navigator echo, thereby minimizing distortion mismatch  
101 between the two echoes.

102 Since one imaging echo presents one segment in multi-shot EPI acquisi-  
103 tion, its effective ESP is defined as

$$\text{ESP}_{\text{eff}} = \frac{\text{ESP}}{R_{\text{in-plane}} \times N_{\text{shot}}} \quad (1)$$

104 Here, a larger number of shots (segments) increases the undersampling factor  
105 per segment (see Fig. 1), but decreases the effective ESP. Since the navigator

106 echo is acquired for each segment, its in-plane undersampling factor equals  
107  $R_{\text{in-plane}}$ . Therefore, the effective ESP of the navigator echo must match that  
108 of the imaging echo, as given in Eq. (1). With a matching effective ESP, the  
109 base resolution of the navigator echo can then be determined.

110 *2.3. In vivo acquisition protocols*

111 We implemented multiple in-vivo acquisition protocols at a clinical 7 T  
112 MR system (MAGNETOM Terra, Siemens Healthineers, Erlangen, Ger-  
113 many) equipped with a 32-channel head coil (Nova Medical, Wilmington,  
114 MA, USA) and the XR-gradient system (maximum gradient strength 80 mT/m  
115 with a peak slew rate of 200 T/m/s). To calibrate coil sensitivity maps, refer-  
116 ence scans employed a gradient-echo (GRE) sequence. Spectral fat saturation  
117 and mono-polar diffusion-encoding gradients were used. The phase-encoding  
118 direction was selected as anterior-to-posterior.

Table 1: NAViEPI acquisition protocols

Protocol	1.0 mm isotropic		sub-millimeter	
	#1	#2	#3	#4
Diffusion mode	MDDW <sup>(1)</sup>		3-scan trace	
Diffusion scheme	monopolar			
Diffusion direction	20	114	3	
<i>b</i> -value (s/mm <sup>2</sup> )	1000	3-shell <sup>(2)</sup>	1000	
<i>b</i> <sub>0</sub>	0	12	1	
FOV (mm <sup>2</sup> )	200	214	220	
In-plane resolution (mm <sup>2</sup> )	1.0		0.5	
Slice thickness (mm)	1.0		2.0	
Slices	141	114	60	
Navigator	No	No	Yes	No
Shots	4	2	5	1
TR (ms)	7700	5200	4400	8000
TEs (ms)	67	66	58/95.1	143
ESP (ms)	1.02	0.81	1.52	1.48
Bandwidth (Hz/Pixel)	1086	1460	758	
Partial Fourier			6/8	
Acceleration <sup>(3)</sup>	1 × 3	3 × 3	3 × 2	
TA (min) <sup>(4)</sup>	10 : 42	22 : 25	1 : 38	0 : 46

<sup>(1)</sup> MDDW: Multi-direction diffusion weighting;

<sup>(2)</sup> 3-shell: 20, 30, and 64 directions with *b*-values of 1000, 2000, and 3000 s/mm<sup>2</sup>, respectively;

<sup>(3)</sup> Acceleration: Both in-plane and slice undersampling can be employed, denoted as (*R*<sub>in-plane</sub> × *R*<sub>slice</sub>);

<sup>(4)</sup> TA: Total acquisition time.

120 This study was approved by the local ethics committee. Three volunteers  
121 with informed consent obtained before scanning participated in this  
122 study. Detailed acquisition protocols are listed in Table 1. In the spirit of re-  
123 producible research, another volunteer with informed consent was recruited  
124 for the scan of all acquisition protocols, and the results were displayed in  
125 Supplementary Information.

126 *2.3.1. 20-diffusion-direction acquisition at 1 mm isotropic resolution*

127 As listed in Table 1, Protocol #1 with four-shot iEPI and without in-  
128 plane undersampling was implemented. This protocol represents the acquisi-  
129 tion scheme employed in many existing multi-shot reconstruction techniques,  
130 (e.g., MUSE, SPA-LLR, and JULEP). The acquired data from this protocol  
131 served as ground truth. Different reconstruction methods, specifically JETS,  
132 MUSE, and JULEP were compared. We compared with JULEP instead of  
133 MUSSELS, because JULEP uses not only structured low-rank constraints  
134 but also explicit phase mapping.

135 We then retrospectively reduced the four-shot data to only one shot per  
136 diffusion encoding without and with the proposed  $k_y$  shifting to simulate  
137 four-fold in-plane undersampling. JETS reconstruction was performed on  
138 the fully-sampled data and the retrospectively undersampled data to validate  
139 the proposed  $k_y$ -shifted acquisition.

140 *2.3.2. Three-shell acquisition at 1 mm isotropic resolution*

141 Protocol #2 in Table 1 was implemented for multi-shell diffusion tensor  
142 imaging (DTI) (Basser et al., 1994). We acquired a total of 114 diffusion  
143 directions, whereas  $b_0$  measurements were interspersed every ten diffusion

<sub>144</sub> directions. This protocol was used to demonstrate the capability of JETS  
<sub>145</sub> in achieving high spatial-angular-temporal resolution.

<sub>146</sub> *2.3.3. 3-scan trace acquisition at  $0.5 \times 0.5 \times 2.0 \text{ mm}^3$  voxel size*

<sub>147</sub> As listed in Table 1, Protocol #3 was implemented based on NAViEPI  
<sub>148</sub> with five shots per diffusion encoding. This protocol was compared against  
<sub>149</sub> single-shot EPI (Protocol #4) with the same spatial resolution and acceler-  
<sub>150</sub> ation, such as to demonstrate the sampling efficiency of NAViEPI.

<sub>151</sub> *2.4. Forward modeling*

<sub>152</sub> Our proposed acquisition method yields multi-dimensional multi-band  
<sub>153</sub>  $k$ -space data  $\mathbf{y}_{c,q,s}$ , where  $c, q, s$  denotes the index of the coil sensitivity  
<sub>154</sub> map, the diffusion encoding, and the shot, respectively. Acquisition modeling  
<sub>155</sub> needs to consider several aspects.

<sub>156</sub> First, the acquired  $k$ -space data  $\mathbf{y}$  is mapped from individual shot images  
<sub>157</sub>  $\mathbf{x}_{q,s,z}$  via the forward model,

$$\begin{aligned} \mathbf{y}_{c,q,s} &= \mathbf{P}_{q,s} \boldsymbol{\Sigma} \boldsymbol{\Theta}_z \mathbf{F} \mathbf{S}_c \mathbf{x}_{q,s,z} \\ \mathbf{y} &:= \mathbf{E}_1 \mathbf{x} \end{aligned} \quad (2)$$

<sub>158</sub> Here, the encoding matrix  $\mathbf{E}_1$  comprises a chain of linear operators. Every  
<sub>159</sub> shot image  $\mathbf{x}$  is point-wise multiplied by a set of coil sensitivity maps ( $\mathbf{S}$ ) and  
<sub>160</sub> Fourier transformed ( $\mathbf{F}$ ). The output is then point-wise multiplied by the  
<sub>161</sub> multi-slice phase map ( $\boldsymbol{\Theta}$ ) with  $z$  the slice index in simultaneously excited  
<sub>162</sub> slices. This operator shifts individual slice along the phase-encoding direction  
<sub>163</sub> via varying phase modulation (Breuer et al., 2005). The SMS  $k$ -space data

164 is then summed (collapsed,  $\Sigma$ ) along the slice dimension and masked (point-  
165 wise multiplied,  $\mathbf{P}$ ) by the sampling pattern of each diffusion encoding and  
166 shot.

167 Second, for diffusion MRI based on multi-shot EPI, multiple shots ac-  
168 quired for a given diffusion encoding need to be combined as one DW image  
169 ( $\tilde{\mathbf{x}}$ ). One possibility is to perform magnitude average (Chen et al., 2013)  
170 or root-sum-squares (RSS) (Mani et al., 2017) of shot images. This method  
171 is robust to in-plane motion, but sub-optimal concerning SNR (Guhaniyogi  
172 et al., 2016). Alternatively, shot combination can be done via shot-to-shot  
173 phase variation correction (Liu et al., 2005; Chen et al., 2013). This can be  
174 incorporated into our formulation as point-wise multiplication between the  
175 shot-to-shot phase variation ( $\Phi$ ) and the DW image ( $\tilde{\mathbf{x}}$ ),

$$\mathbf{x}_{q,s,z} = \Phi_{q,s,z} \tilde{\mathbf{x}}_{q,z} \quad (3)$$

176 Note that  $\tilde{\mathbf{x}}$  can be obtained by applying the adjoint of  $\Phi$  to  $\mathbf{x}$ . In MUSE,  
177  $\Phi$  is obtained by parallel imaging reconstruction of all shots with subsequent  
178 phase smoothing of every shot image. Based on this phase correction, the  
179 complete forward model follows

$$\mathbf{y} := \mathbf{E}_2 \tilde{\mathbf{x}} = \mathbf{E}_1 \Phi \tilde{\mathbf{x}} \quad (4)$$

180 where the encoding matrix  $\mathbf{E}_2$  comprises the chain of the shot-to-shot phase  
181 variation  $\Phi$  and the encoding matrix  $\mathbf{E}_1$ . We implemented these two encoding  
182 operators in SigPy (Ong and Lustig, 2019).

### 183 2.5. Joint $k$ - $q$ -slice reconstruction

184 Based on the generalized forward models in Eqs. (2) and (4), our proposed  
185 joint  $k$ - $q$ -slice reconstruction can be formulated as a three-step approach.

186     **I. Navigator echo reconstruction.** The acquisition of navigator echoes  
 187     follows the forward model in Eq. (2), so the reconstruction of navigator  
 188     echoes can be formulated as:

$$\operatorname{argmin}_{\mathbf{x}} \|\mathbf{y} - \mathbf{E}_1 \mathbf{x}\|_2^2 + \lambda \mathbf{R}(\mathbf{x}) \quad (5)$$

189     where  $\mathbf{R}(\mathbf{x})$  denotes the regularization functional with the regularization  
 190     strength  $\lambda$ . In this work,  $\ell^2$  regularization was used, i.e.,  $\mathbf{R}(\mathbf{x}) =$   
 191      $\|\mathbf{x}\|_2^2$ . In the case of self-navigating (i.e., no navigator acquired) as Pro-  
 192     tocol #2, the central  $k$ -space region (i.e., 1/4 of the full image matrix)  
 193     of each segment is used as  $\mathbf{y}$  in Eq. (5).

194     **II. Phase smoothing.** Shot-to-shot phase variation was extracted from  
 195     the reconstructed navigator echo phases. Assuming that phase images  
 196     are spatially smooth (Chen et al., 2013; Dai et al., 2023), we employed  
 197     the adaptive Hanning filter to smooth shot phases,

$$\mathbf{x} = \mathbf{F}^{-1} \mathcal{H}^K \mathbf{F} \mathbf{x} \quad (6)$$

198     where  $x$  is the reconstructed navigator image from Step I.  $\mathcal{H}$  is the  
 199     Hanning window with the non-negative integer  $K$ .  $K$  controls the width  
 200     of the Hanning window.

201     **III. Shot-combined reconstruction.** Joint reconstruction of all DW im-  
 202     ages using the shot-combined forward model  $\mathbf{E}_2$  with shot-to-shot phase  
 203     variation from Step II reads:

$$\operatorname{argmin}_{\tilde{\mathbf{x}}} \|\mathbf{y} - \mathbf{E}_2 \tilde{\mathbf{x}}\|_2^2 + \lambda \|\mathbf{T}(\tilde{\mathbf{x}})\|_* \quad (7)$$

204     Here, LLR regularization was employed in the local spatial-diffusion  
 205     matrices, based on the theory of partially separable functions (Liang,

206        2007; Trzasko and Manduca, 2011; Zhang et al., 2015).  $\mathbf{T}$  represents  
207        a linear operator that firstly slides a local patch window through all  
208        DW images and then flattens every set of local patches to construct  
209        two-dimensional (2D) spatial-diffusion matrices. The spatial dimension  
210        equals the block size, and the diffusion dimension is the number of dif-  
211        fusion encodings.  $\|\mathbf{T}(\tilde{\mathbf{x}})\|_*$  is the nuclear norm, i.e. the sum of singular  
212        values of a spatial-diffusion matrix. This nuclear norm regularization  
213        was accomplished via singular value thresholding (SVT) of each spatial-  
214        diffusion matrix (Cai et al., 2010). After SVT, the adjoint of  $\mathbf{T}$ ,  $\mathbf{T}^H$ ,  
215        was needed to reorder pixel values from the spatial-diffusion matrices  
216        back to DW images.

217        To alleviate checkerboard artifacts induced by LLR regularization with  
218        non-overlapping blocks (Hu et al., 2020), we employed overlapping blocks.  
219        In this case, values from overlapping positions are summed up to the  
220        output of  $\mathbf{T}^H$ . To enable the correct use of  $\mathbf{T}^H$ , we element-wise divided  
221        the output of  $\mathbf{T}^H$  by a scaling matrix. This matrix was obtained via  
222         $\mathbf{T}^H(\mathbf{T}(\mathbf{1}))$ , where  $\mathbf{1}$  denotes the matrix of all ones with the same shape  
223        as the input  $\mathbf{x}$ .

224        As the local patch window varies depending on the number of diffusion  
225        encodings or user selection, we implemented a singular-value spectrum  
226        normalization strategy to reduce the effect of the local patch window  
227        variation on regularization strength. Specifically, the singular values of  
228        constructed spatial-diffusion matrices were divided by the patch window  
229        width. After SVT, the thresholded singular values were multiplied with  
230        the patch window width for rescaling.

231    2.6. Reconstruction

232    The acquired raw data was read in by twixtools (<https://github.com/pehses/twixtools>). Ramp-sampling regridding and FOV/2-ghost correction were also performed in twixtools. Subsequently, coil sensitivity maps were computed from reference scans using ESPIRiT (Uecker et al., 2014) in SigPy (Ong and Lustig, 2019).

237    With this pre-processing as well as the implemented forward models and proximal operator, the inverse problem in Eq. (7) was solved by the alternating direction method of multipliers (ADMM) (Boyd et al., 2010).

240    ADMM solves the minimization problems in an alternating update scheme,

$$\begin{cases} \mathbf{x}^{(k+1)} := \underset{\mathbf{x}}{\operatorname{argmin}} \| \mathbf{y} - \mathbf{E}(\mathbf{x}) \|^2 + \rho/2 \| \mathbf{T}\mathbf{x} - \mathbf{z}^{(k)} + \mathbf{u}^{(k)} \|_2^2 \\ \mathbf{z}^{(k+1)} := \mathcal{T}_{\lambda/\rho}(\mathbf{T}\mathbf{x}^{(k+1)} + \mathbf{u}^{(k)}) \\ \mathbf{u}^{(k+1)} := \mathbf{u}^{(k)} + \mathbf{T}\mathbf{x}^{(k+1)} - \mathbf{z}^{(k+1)} \end{cases} \quad (8)$$

241    where  $k$  denotes the ADMM iteration.  $\mathbf{z}$  is the auxiliary variable ( $\mathbf{z} = \mathbf{T}\mathbf{x}$ ), and  $\mathbf{u}$  is the Lagrangian multipliers. Importantly, when solving Eq. (2),  $\mathbf{x}$  denotes shot images and  $\mathbf{E}$  denotes  $\mathbf{E}_1$  in Eq. (8). In contrast,  $\mathbf{x}$  denotes shot-combined images and  $\mathbf{E}$  denotes  $\mathbf{E}_2$  when solving Eq. (4).  $\mathbf{x}$  can be solved using linear least square algorithms, e.g. conjugate gradients (Hestenes and Stiefel, 1952), while  $\mathbf{z}$  is updated via singular value thresholding ( $\mathcal{T}$ ) with the thresholding parameter  $\lambda/\rho$ . The coupling parameter  $\rho$  is effective in both the update of  $\mathbf{x}$  and  $\mathbf{z}$ . It acts as Tikhonov regularization strength when updating  $\mathbf{x}$ , but also inversely scales the thresholding strength when updating  $\mathbf{z}$ .

251    In this work, 15 ADMM iterations with  $\rho = 0.05$  and  $\lambda = 0.01$  were used.

252 All reconstructions were done on a single A100 SXM4/NVLink GPU with  
253 40 GB memory (NVIDIA, Santa Clara, CA, USA).

254 We compared our proposed joint reconstruction with established multi-  
255 shot reconstruction techniques, specifically, MUSE (Chen et al., 2013) and  
256 JULEP (Dai et al., 2023), hosted on GitHub by Dr. Dai (Dai et al., 2023).  
257 Further, we performed the local-PCA denoising (Cordero-Grande et al., 2019)  
258 as implemented in MRtrix (Tournier et al., 2019) on the MUSE reconstructed  
259 complex DW images.

260 The in vivo data acquired from Protocol #2 in Table 1 consisted of 126  
261 diffusion directions, which exceeds the available GPU memory. Therefore,  
262 the 126 data volumes were uniformly split into three parts for our JETS  
263 reconstruction with a LLR block width of 6 and the LLR regularization in  
264 both Steps I and III in Section 2.5. In addition, MUSE reconstruction was  
265 also performed, followed by the local-PCA denoising. Reconstructed DWIs  
266 were then processed by DiPy (Garyfallidis et al., 2014) to obtain color-coded  
267 fractional anisotropy (cFA) maps.

268    **3. Results**

269    *3.1. Smoothing of shot-to-shot phase variation*

270    Navigators were acquired with the acceleration rate as listed in Table 1.  
271    Besides, the base resolution of navigators (e.g. 32 in Protocol #3 in Table 1)  
272    was smaller than imaging echoes. As a result, reconstructed navigator phases  
273    (refer to the first column in Fig. 3) from Step I in Section 2.5 are not spatially  
274    smooth. Such phases, when used in the shot-combined reconstruction, result  
275    in signal void artifacts in DW images. To address this problem, we utilized  
276    the phase smoothing procedure. As shown in Fig. 3, the ripple-like phase  
277    artifact disappears at  $K = 5$ , while retaining the shot-to-shot phase variation.  
278    In contrast, a larger  $K$  (e.g.,  $K = 20$ ) makes the filter too strong and partially  
279    removes phase variation.

280    *3.2. Comparison to MUSE and JULEP with four-shot iEPI acquisition*

281    The iterative phase smoothing was also applicable to MUSE-type self-  
282    navigating reconstruction, where shot phases were reconstructed from imag-  
283    ing echoes. Fig. 4 compares our proposed JETS with MUSE (Chen et al.,  
284    2013), MUSE with complex-valued local-PCA denoiser (Cordero-Grande et al.,  
285    2019), and JULEP (Dai et al., 2023). The residual noise from MUSE can be  
286    largely removed by the denoiser. However, when compared to JETS, the de-  
287    noiser shows residual noise patterns within the globus pallidus (indicated by  
288    the red arrow). JETS also shows better denoising than JULEP. The reason  
289    is that JETS enforces spatial-diffusion regularization, whereas JULEP for-  
290    mulates structured low-rank regularization of the four shots for one diffusion  
291    encoding.

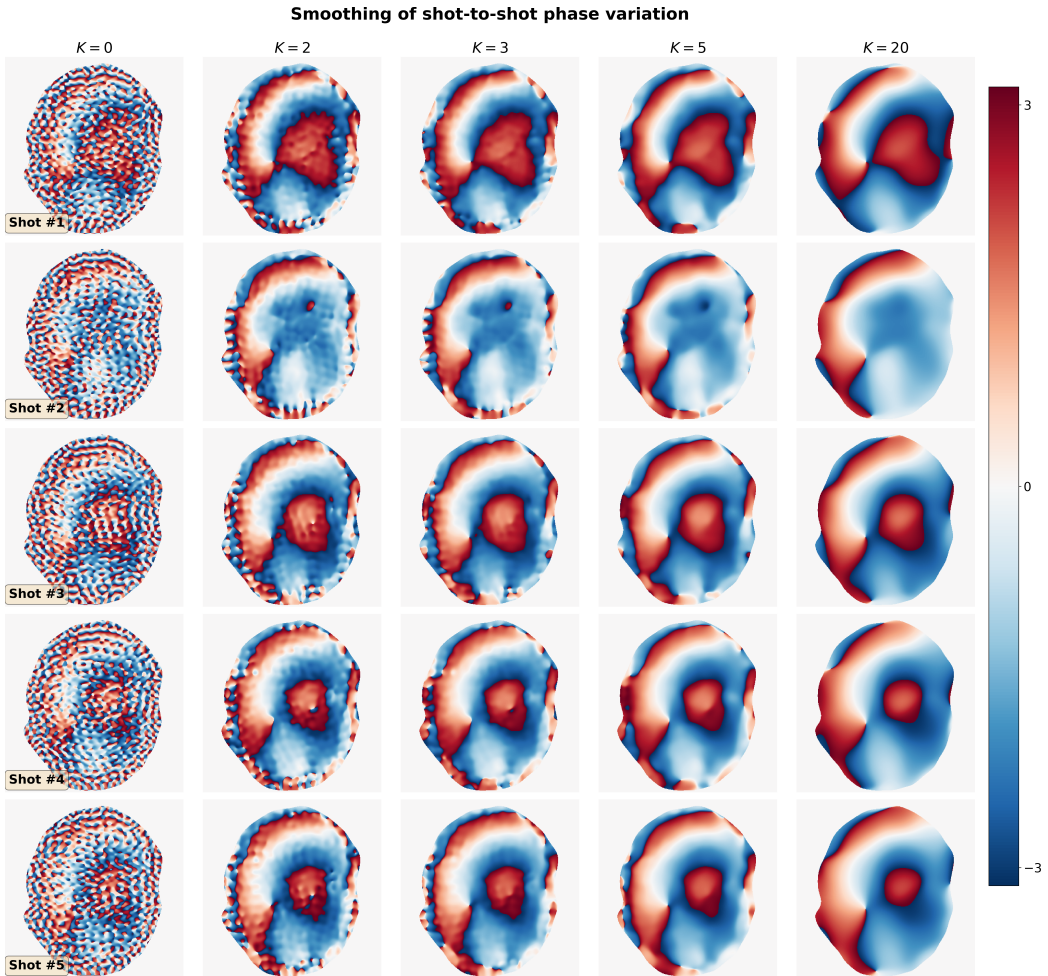


Figure 3: Smoothing of shot-to-shot phase variation according to Eq. (6). Navigators from Protocol #3 were reconstructed based on Step I in Section 2.5 and then used as the input (the column with  $K = 0$ ).

**8th DW image from 4-shot iEPI @ 1 mm ISO**

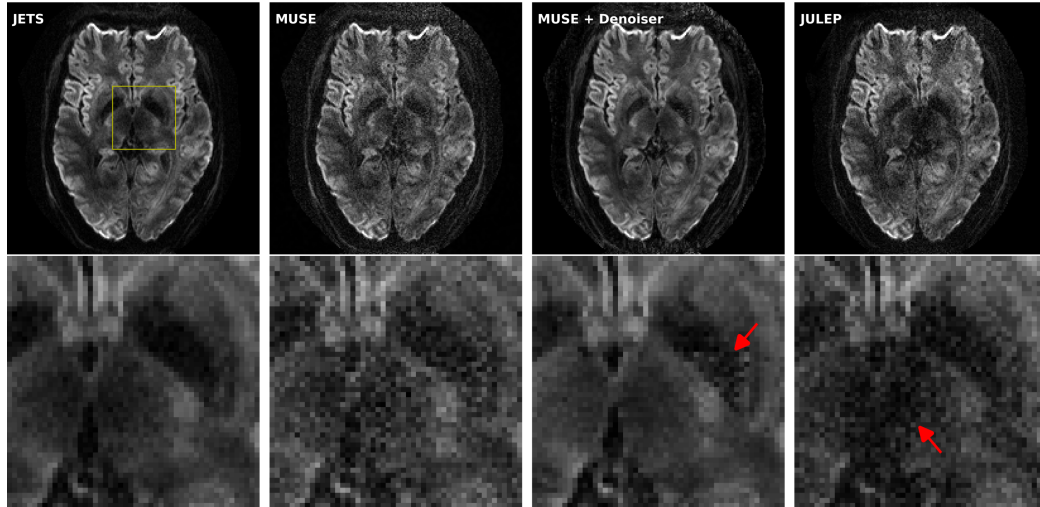


Figure 4: Reconstructed DW images (the 8th diffusion encoding) based on 4-shot iEPI acquisition with 1 mm isotropic resolution (Protocol #1 in Table 1). Four reconstruction methods are compared (from left to right): JETS, MUSE, MUSE with denoiser, and JULEP. The 2nd row displays the magnified views of the yellow square. The image from the denoiser (3rd column) shows residual noise patterns within the globus pallidus (indicated by the red arrow). The JULEP reconstruction (4th column) shows signal dropout in the central region (indicated by the red arrow).

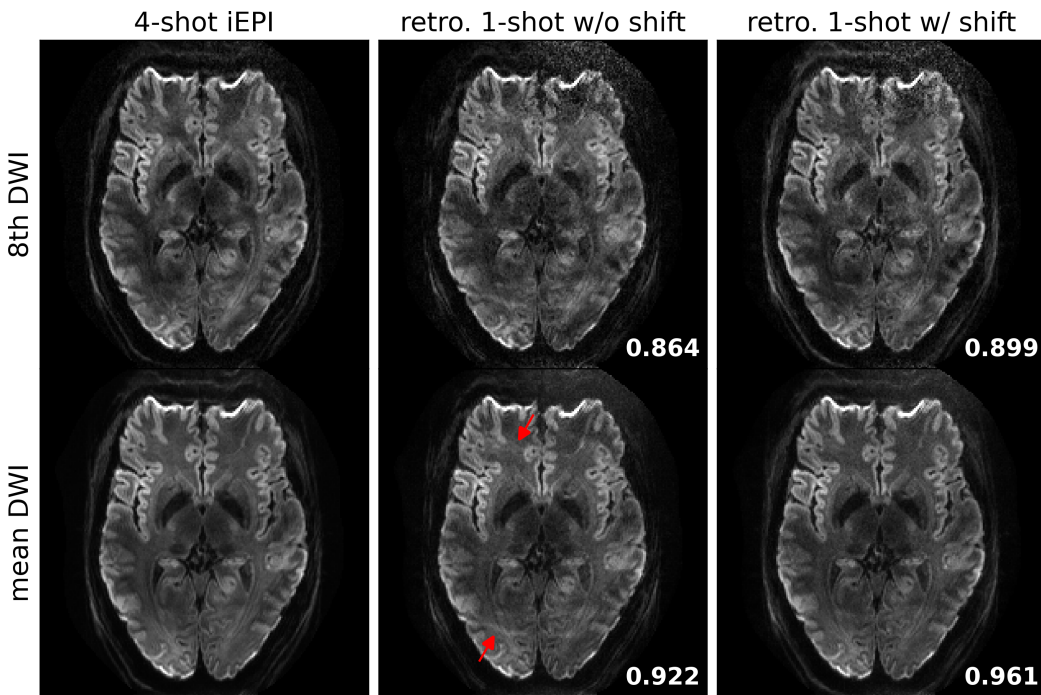


Figure 5: Quantitative validation of the proposed  $k_y$ -shift encoding sampling pattern based on 4-shot iEPI acquisition with 1 mm isotropic resolution (Protocol #1 in Table 1). (Top) the 8th diffusion encoding and (bottom) mean DWI over 20 diffusion encodings. (1st column) JETS reconstruction of 4-shot iEPI acquisition is used as the ground truth. The 2nd and the 3rd column displays JETS reconstruction of retrospectively undersampled 1-shot acquisition without and with  $k_y$  shifting, respectively. Residual aliasing artifacts are visible in the reconstruction without  $k_y$  shifting, as indicated by the red arrows. Structural similarity (SSIM) values are computed and displayed in the bottom right corners.

292    3.3. Retrospectively undersampling from the four-shot iEPI acquisition

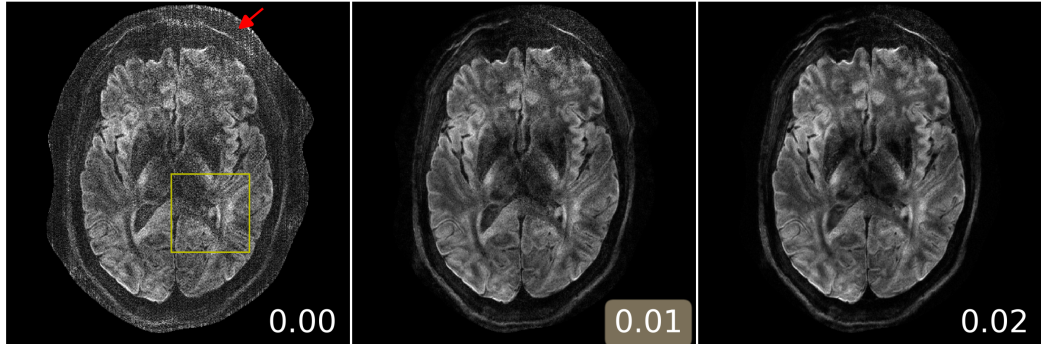
293    JETS reconstruction results on the four-shot prospectively fully-sampled  
294    data from Protocol #1 in Table 1, as well as on the retrospectively under-  
295    sampled one-shot data without and with the proposed  $k_y$  shift are displayed  
296    in Fig. 5. Residual aliasing artifacts are visible in the reconstruction with-  
297    out  $k_y$  shifting, as indicated by the red arrows. In contrast, the  $k_y$  shifting  
298    scheme supplies a complementary  $k$ - $q$ -space sampling pattern, which is bene-  
299    ficial for joint reconstructions such as JETS. As shown in Fig. 5, JETS results  
300    in improved SSIM values and reduced aliasing artifacts, when compared to  
301    the reconstruction without  $k_y$  shifting. Figs. 4 and 5 show a slice containing  
302    the globus pallidus with strong  $T_2$ -weighted contrast and highlighting the  
303    advantage of  $k_y$ -shift encoding in reducing undersampling artifacts.

304    3.4. Analysis of reconstruction parameters

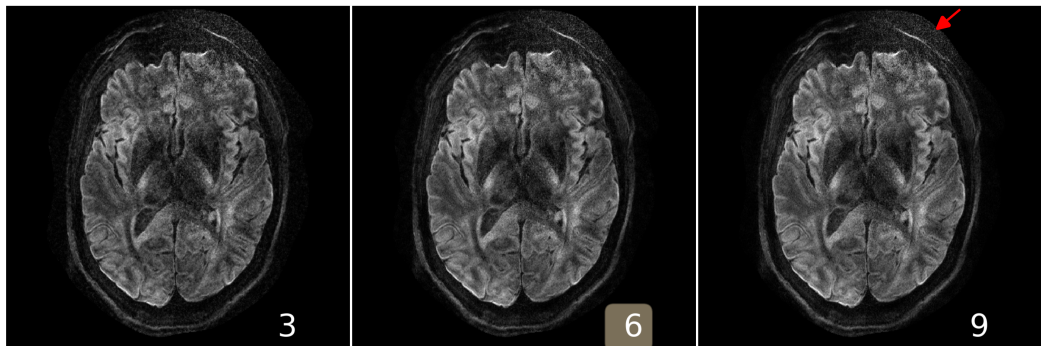
305    Here we provide a systematic analysis of the proposed JETS reconstruc-  
306    tion with LLR regularization applied to the spatial-diffusion dimension, as  
307    shown in Fig. 6.

308    First, we varied the regularization strength  $\lambda$ . We tested values of 0, 0.01,  
309    and 0.02. The reconstruction with  $\lambda = 0$  in Eq. (7) corresponds to parallel  
310    imaging reconstruction without LLR regularization. It is worth noting that  
311    the proposed NAViEPI sequence demonstrates high-quality sub-millimeter  
312    DW images ( $0.5 \times 0.5 \times 2.0$  mm $^3$  in this example). The DW images can be  
313    further improved with the use of LLR regularization, i.e., reduced noise, as  
314    seen in the reconstruction with  $\lambda = 0.01$ . Increasing  $\lambda$  (e.g. 0.02) further  
315    reduces noise, but at the cost of increased blurring. Therefore,  $\lambda = 0.01$  was  
316    selected in this work.

**(A) varying  $\lambda$ , keeping block as 6 and stride as 1**



**(B) varying block width, keeping  $\lambda$  0.01 and stride as 1**



**(C) varying stride, keeping  $\lambda$  as 0.01 and block as 6**

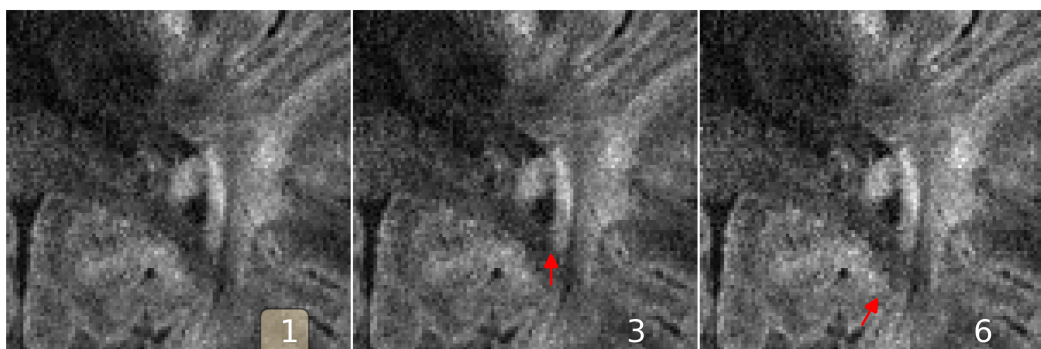


Figure 6: Analysis of reconstruction parameters based on the 3-scan trace acquisition with  $0.5 \times 0.5 \times 2.0 \text{ mm}^3$  (Protocol #3 in Table 1). Displayed are JETS reconstructed single-direction DW images. **(A)** Varying the regularization strength  $\lambda$  from 0 to 0.01 and 0.02. **(B)** Varying the block width from 3 to 6 and 9. The red arrow indicates increased noise with the large block width. **(C)** Varying the stride size from 1 to 3 (partially overlapping) and 6 (non-overlapping). The red arrows indicate blocky artifacts.

317 Second, besides the regularization strength, we varied the block width.  
318 Reconstruction results for the data from Protocols #3 and #2 in Table 1 are  
319 displayed in Fig. 6 (B) and Supporting Information Figure S6, respectively.  
320 With the above-mentioned normalization strategy, the reconstruction results  
321 show similar denoising effects. However, small block width (i.e., 3) suffers  
322 from residual blurring artifacts, as shown in SI Figure S6. Therefore, the  
323 block width of 6 was selected in this work.

324 Third, we varied the stride, i.e., the step from one local patch to the  
325 next. The use of overlapping LLR (Fig. 6 (C) left) better suppresses blocky  
326 artifacts, compared to the partially overlapping (stride < block) LLR (Fig. 6  
327 (C) middle) and the non-overlapping (stride = block) LLR (Fig. 6 (C) right).

328 *3.5. Sampling efficiency of NAViEPI*

329 As shown in Fig. 7, NAViEPI achieves sub-millimeter resolution (voxel  
330 size  $0.5 \times 0.5 \times 2.0 \text{ mm}^3$ ) with the use of a 5-shot acquisition. When compared  
331 to a single-shot acquisition with the same voxel size, the acquisition time of  
332 NAViEPI is about two times longer, but the image quality of NAViEPI is  
333 remarkably improved.

334 In the sub-millimeter imaging scenario, the increased base resolution re-  
335 quires longer TE (143 ms) in the single-shot acquisition, which results in  
336 significant signal loss due to  $T_2$  relaxation. Therefore, sub-millimeter DWI  
337 necessitates multi-shot acquisition, which is subject to shot-to-shot phase  
338 variation and long scan time. However, NAViEPI solves both challenges. The  
339 5-shot acquisition reduces TE to 58 ms, and thus retains SNR significantly  
340 compared to the single-shot acquisition. Moreover, the JETS reconstruction  
341 can help to reduce noise and improve structural visibility.

**3-scan trace acquisition with voxel size  $0.5 \times 0.5 \times 2.0 \text{ mm}^3$**

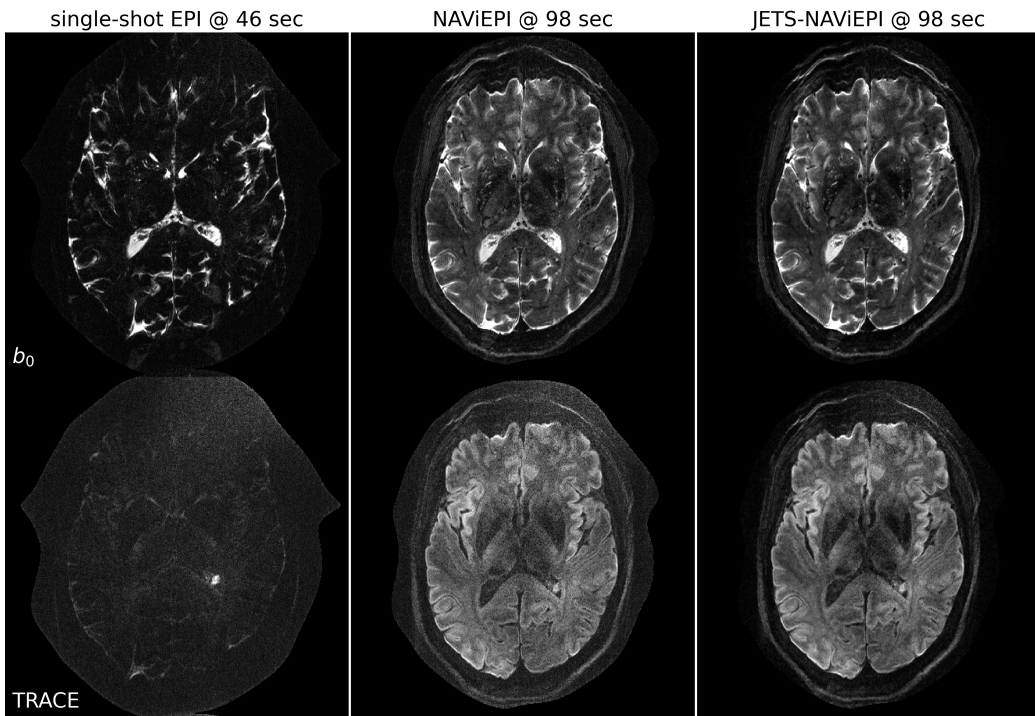


Figure 7: Sampling efficiency of the proposed NAViEPI sequence. 5-shot NAViEPI acquisition with the voxel size  $0.5 \times 0.5 \times 2.0 \text{ mm}^3$  (Protocol #3) was compared with single-shot EPI acquisition (Protocol #4). Both the 1st and the 2nd columns were reconstructed via parallel imaging without LLR regularization, whereas the 3rd column was reconstructed via JETS.

**3-scan trace acquisition with voxel size  $0.5 \times 0.5 \times 2.0 \text{ mm}^3$**

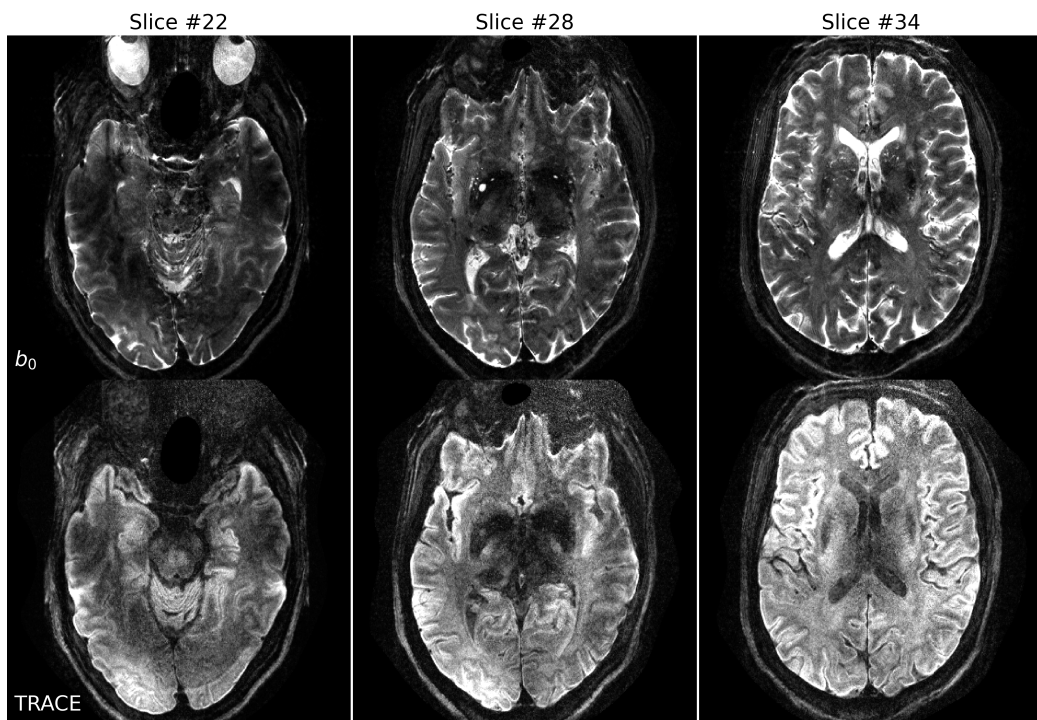


Figure 8: Reconstruction of the 3-scan trace acquisition with the voxel size  $0.5 \times 0.5 \times 2.0 \text{ mm}^3$  (Protocol #3) at different slices.

342 Fig. 8 shows the JETS reconstructed  $b_0$  and TRACE images in different  
343 slice locations. Admittedly, the lower brain region (e.g. slice #22) exhibits in-  
344 homogeneous and lower signal intensity than the upper slices. Such inhomog-  
345 eneity can be alleviated with the use of multi-channel parallel transmission  
346 (Katscher et al., 2003; Grissom et al., 2010).

347 Here, Figs. 6 and 7 show a slice with a benign lesion (the circular bright  
348 spot) within the left ventricle. Fig. 8 displays three representative slices:  
349 (left) an inferior brain region with marked  $B_1^+$  field inhomogeneity, (mid-  
350 dle) the middle brain slice which shows susceptibility artifacts in the frontal  
351 region, and (right) a superior brain slice which shows the ventricle.

352 *3.6. Diffusion tensor imaging*

353 Protocol #2 in Table 1 yields an acceleration factor of  $6 \times 3$  per shot, re-  
354 sulting in severe noise amplification in MUSE reconstructed DWIs, as shown  
355 in Fig. 9. Here, a slice that highlights the corpus callosum is displayed, and  
356 the diffusion direction at the  $b$ -value of  $3000 \text{ s/mm}^2$  with bright signal within  
357 the corpus callosum is shown. The local-PCA denoiser substantially removes  
358 noise, but the DWI at high  $b$ -values still illustrates more noise, compared to  
359 the proposed JETS reconstruction. On the other hand, we applied the local-  
360 PCA denoiser before the shot combination in MUSE. As shown in Fig. 9,  
361 this approach is less effective compared to the application of the denoiser  
362 after the shot combination, because shot images were reconstructed from the  
363 central  $k$ -space region and have a coarse resolution.

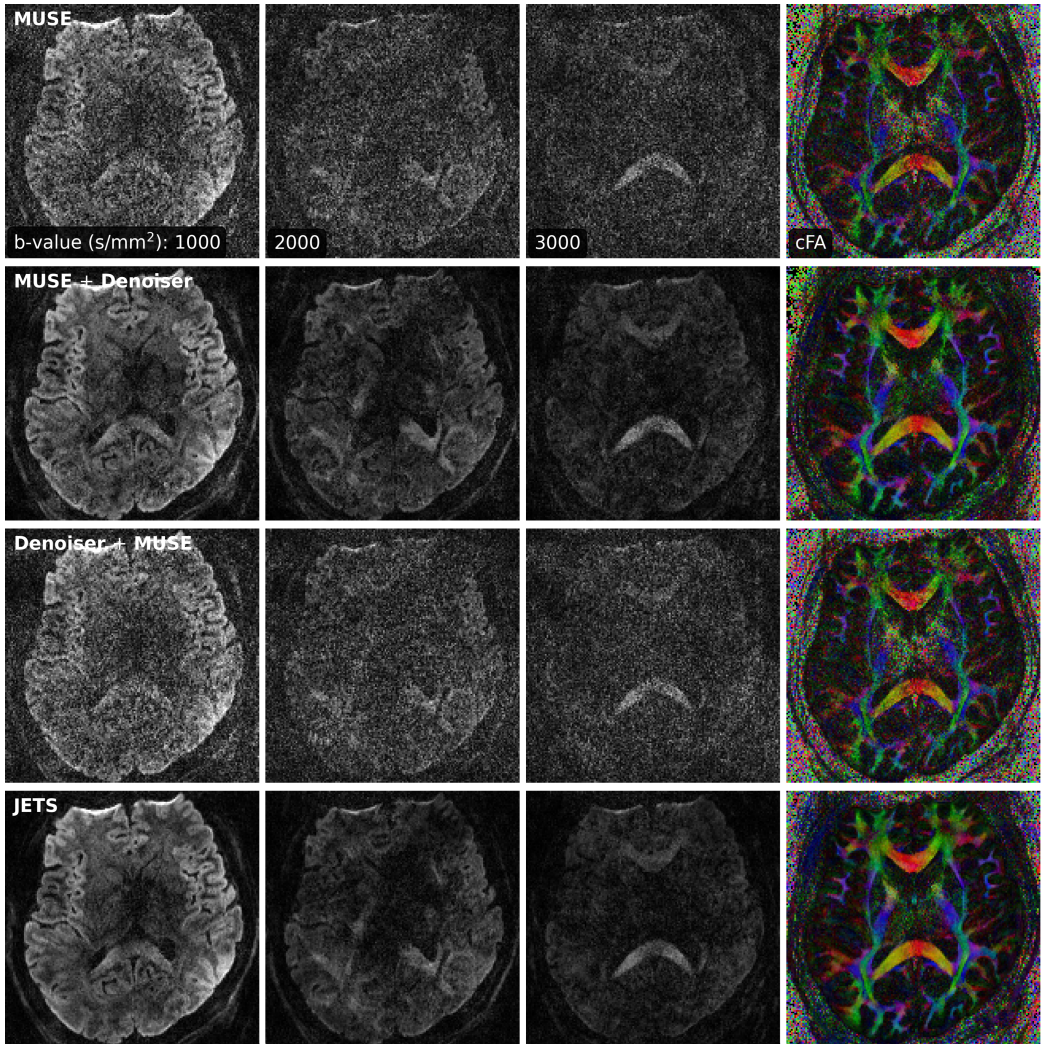


Figure 9: Comparison of three-shell DWIs and cFA maps with data acquired by Protocol #2 in Table 1. Reconstruction methods from top to bottom were MUSE, MUSE with the local-PCA denoiser, the application of the denoiser on shot images before the shot combination in MUSE, and the proposed JETS method.

364 **4. Discussion**

365 This work reports a novel DW-MRI technique, JETS-NAViEPI. NAViEPI  
366 (1) achieves the fast and efficient acquisition of both imaging and navigator  
367 echoes, (2) enforces consistent effective ESP between the two echoes, and (3)  
368 allows for undersampled iEPI as well as a large number of shots. Moreover,  
369 compared to the single-shot acquisition, joint  $k$ - $q$ -slice reconstruction with  $k_y$ -  
370 shift encoding on NAViEPI retains SNR and reduces aliasing artifacts in DW  
371 images. As a result, JETS-NAViEPI renders high spatiotemporal resolution  
372 diffusion MRI protocols in 7 T, e.g., a 3-scan trace acquisition with the voxel  
373 size  $0.5 \times 0.5 \times 2.0 \text{ mm}^3$  at 1.5 min.

374 One limitation of JETS-NAViEPI is the long reconstruction time due to  
375 the simultaneous reconstruction of all DW images and the use of overlapping  
376 locally low-rank regularization. The reconstruction for the Protocol #3 in  
377 Table 1 on an A100 GPU takes about 2 min per multi-band slice. To reduce  
378 the computation time, coil compression algorithms (Buehrer et al., 2007;  
379 Huang et al., 2008) can be employed to reduce the number of coils for image  
380 reconstruction. Moreover, one can deploy multi-GPU distributed computing  
381 or modern optimization algorithms (e.g. stochastic gradient descent) (Ong  
382 et al., 2020) to speed up the reconstruction.

383 Neither the signal modeling in Eqs. (2) and (4) nor the LLR regulariza-  
384 tion considers the subject motion. In the presence of motion, the regularized  
385 reconstruction can degrade. To overcome this problem, scout-informed mo-  
386 tion estimation and reconstruction (Polak et al., 2022) could be integrated  
387 into the framework.

388 Another potential extension of this work is to incorporate distortion cor-

389 rection. The standard distortion correction method is known as TOPUP  
390 ([Andersson et al., 2003](#)), which acquires two scans with opposing phase-  
391 encoding directions to obtain the field inhomogeneity map and then per-  
392 forms conjugate phase reconstruction to correct for distortion. Alternatively,  
393 a multi-echo acquisition could be used for the coil sensitivity reference scan,  
394 such that both coil sensitivity and  $B_0$  field inhomogeneity maps could be  
395 reconstructed from the data.

396 This work employed a single regularization weight  $\lambda$  to enforce low rank-  
397 ness along the spatial-diffusion direction. However, SNR may be heteroge-  
398 neous within the FOV. Therefore, one single regularization scalar may be  
399 inadequate to cover the whole FOV. Beyond this SVT-based reconstruction,  
400 one can seek to use machine learning to learn a  $q$ -space prior as the regularizer  
401 ([Hammernik et al., 2018; Lam et al., 2019; Mani et al., 2021](#)).

402 Although NAViEPI employs navigators for the acquisition of shot-to-  
403 shot phase variation, it is worth noting that phase behavior depends on  
404 several hard-to-control factors such as pulsatile motion, bulk motion, loca-  
405 tions within the brain, and diffusion sensitization strength. Therefore, more  
406 comprehensive modeling or post-processing such as image registration can  
407 be considered in future work.

408 This work compared LLR regularized JETS to MUSE post-processed by  
409 the local PCA denoiser ([Cordero-Grande et al., 2019](#)). Both the LLR reg-  
410 ularization and the local PCA denoiser are based on the principle that low  
411 rankness exists in the spatial-diffusion dimension ([Moeller et al., 2021](#)), where  
412 the spatial content is extracted from local patches within the full image vol-  
413 ume and the diffusion dimension is from the  $q$ -space encoding. One could

414 integrate the automatic noise estimation based on the Marchenko-Pastur law  
415 for the determination of the thresholds in the LLR regularization to synergize  
416 these two methods.

417 While this work reconstructs all DW images and then performs model  
418 fitting, an alternative approach is to directly estimate  $b_0$  and diffusion ten-  
419 sors from measured  $k$ - $q$ -space data using model-based reconstruction (Knoll  
420 et al., 2015; Dong et al., 2018; Shafieizargar et al., 2023). Compared to DW  
421 image reconstruction, model-based reconstruction solves for a fewer number  
422 of unknowns, but requires strict diffusion tensor modeling and the use of  
423 nonlinear least square solvers.

424 **5. Conclusions**

425 We demonstrated the JETS-NAViEPI technique, which integrates a  $k_y$ -  
426 shifted encoding navigator-based interleaved EPI sequence and joint recon-  
427 struction with overlapping locally low-rank regularization for high spatial-  
428 angular-temporal resolution DW-MRI at 7 T. This technique allows for high-  
429 quality DW image reconstruction with accelerated acquisitions.

430 **Data and code available statement**

431 In the spirit of reproducible and open science, we publish our source code  
432 (<https://github.com/ZhengguoTan/sigpy>) as well as the raw  $k$ -space data  
433 (<https://doi.org/10.5281/zenodo.10474402>). We also provide interac-  
434 tive demonstrations of the reconstruction procedure (<https://github.com/>  
435 [ZhengguoTan/NAViEPI](https://github.com/ZhengguoTan/NAViEPI)).

436 **Author contributions**

437 Z.T.: Conceptualization, Methodology, Data Acquisition, Software, Vi-  
438 sualization, Writing (original draft preparation, review and editing); P.A.L.:  
439 Conceptualization, Methodology, Data Acquisition, Software, Writing (re-  
440 view and editing); R.M.H.: Conceptualization, Methodology, Writing (review  
441 and editing), Supervision; F.B.L.: Conceptualization, Methodology, Writing  
442 (review and editing), Supervision, Funding acquisition; F.K.: Conceptual-  
443 ization, Methodology, Writing (review and editing), Supervision, Funding  
444 acquisition.

445 **Funding information**

446 Funding by the German Research Foundation (DFG) is gratefully ac-  
447 knowledged (projects 513220538, 512819079; and project 500888779 of the  
448 RU5534 MR biosignatures at UHF). In addition, funding by the National  
449 Institutes of Health (NIH), R01 EB024532 and P41 EB017183, is gratefully  
450 acknowledged.

451 In addition, we gratefully acknowledge the scientific support and HPC  
452 resources provided by the Erlangen National High Performance Computing  
453 Center (NHR@FAU) of Friedrich-Alexander-University Erlangen-Nuremberg  
454 (FAU) under the NHR project b143dc. NHR funding is provided by federal  
455 and Bavarian state authorities. NHR@FAU hardware is partially funded by  
456 the German Research Foundation (DFG) – 440719683.

457 **Declaration of competing interests**

458 P.A.L. and R.M.H. are Siemens Healthcare employees. The remaining  
459 authors declare no competing interests.

460 **Acknowledgments**

461 The authors thank Dr. Peter Neher for the discussion on MITK-Diffusion.  
462 The authors thank Dr. Berkin Bilgic for making the MUSSELS source code  
463 (<https://bit.ly/2QgBg9U>) publically available, Dr. Erpeng Dai for sharing  
464 the JULEP source code (<https://github.com/daiep/JULEP>) on GitHub,  
465 and Dr. Zhiyong Zhang for sharing the SPA-LLR source code (<https://github.com/ZZgroupSJTU/PMCmsDTI>) on GitHub. The authors also thank  
466 Dr. Philipp Ehses for the discussion on twixtools (<https://github.com/pehses/twixtools>).  
467

469 **References**

- 470 Andersson, J.L.R., Skare, S., Ashburner, J., 2003. How to correct suscepti-  
471 bility distortions in spin-echo echo-planar images: application to diffusion  
472 tensor imaging. NeuroImage 20, 870–888. doi:[10.1016/S1053-8119\(03\)00336-7](https://doi.org/10.1016/S1053-8119(03)00336-7).  
473
- 474 Bammer, R., Keeling, S.L., Augustin, M., Pruessmann, K.P., Wolf, R., Stoll-  
475 berger, R., Hartung, H.P., Fazekas, F., 2001. Improved diffusion-weighted  
476 single-shot echo-planar imaging (EPI) in stroke using sensitivity encoding  
477 (SENSE). Magn. Reson. Med. 46, 548–554. doi:[10.1002/mrm.1226](https://doi.org/10.1002/mrm.1226).

- 478 Basser, P.J., Mattiello, J., Le Bihan, D., 1994. MR diffusion tensor  
479 spectroscopy and imaging. *Biophys. J.* 66, 259–267. doi:[10.1016/S0006-3495\(94\)80775-1](https://doi.org/10.1016/S0006-3495(94)80775-1).
- 481 Bilgic, B., Chatnuntawech, I., Manhard, M.K., Tian, Q., Liao, C., Iyer, S.S.,  
482 Cauley, S.F., Huang, S.Y., Polimeni, J.R., Wald, L.L., Setsompop, K.,  
483 2019. Highly accelerated multishot echo planar imaging through synergistic  
484 machine learning and joint reconstruction. *Magn. Reson. Med.* 82, 1343–  
485 1358. doi:[10.1002/mrm.27813](https://doi.org/10.1002/mrm.27813).
- 486 Block, K.T., Uecker, M., Frahm, J., 2007. Undersampled radial MRI with  
487 multiple coils. Iterative image reconstruction using a total variation con-  
488 straint. *Magn. Reson. Med.* 57, 1186–1098. doi:[10.1002/mrm.21236](https://doi.org/10.1002/mrm.21236).
- 489 Boyd, S., Parikh, N., Chu, E., Peleato, B., Eckstein, J., 2010. Distributed  
490 optimization and statistical learning via the alternating direction method  
491 of multipliers. *Foundations and Trends in Machine Learning* 3, 1–122.  
492 doi:[10.1561/2200000016](https://doi.org/10.1561/2200000016).
- 493 Breuer, F.A., Blaimer, M., Heidemann, R.M., Mueller, M.F., Griswold, M.A.,  
494 Jakob, P.M., 2005. Controlled aliasing in parallel imaging results in higher  
495 acceleration (CAIPIRINHA) for multi-slice imaging. *Magn. Reson. Med.*  
496 53, 684–691. doi:[10.1002/mrm.20401](https://doi.org/10.1002/mrm.20401).
- 497 Buehrer, M., Pruessmann, K.P., Boesiger, P., Kozerke, S., 2007. Array com-  
498 pression for MRI with large coil arrays. *Magn. Reson. Med* 57, 1131–1139.  
499 doi:[10.1002/mrm.21237](https://doi.org/10.1002/mrm.21237).

- 500 Butts, K., Riederer, S.J., Ehman, R.L., Thompson, R.M., Jack, C.R., 1993.  
501 Interleaved echo planar imaging on a standard MRI system. Magn. Reson.  
502 Med. 31, 67–72. doi:[10.1002/mrm.1910310111](https://doi.org/10.1002/mrm.1910310111).
- 503 Cai, J.F., Candès, E.J., Shen, Z., 2010. A singular value thresholding  
504 algorithm for matrix completion. SIAM. J. Optim. 20, 1956–1982.  
505 doi:[10.1137/080738970](https://doi.org/10.1137/080738970).
- 506 Chen, N.K., Guidon, A., Chang, H.C., Song, A.W., 2013. A robust multi-  
507 shot scan strategy for high-resolution diffusion weighted MRI enabled by  
508 multiplexed sensitivity-encoding (MUSE). NeuroImage 72, 41–47. doi:[10.1016/j.neuroimage.2013.01.038](https://doi.org/10.1016/j.neuroimage.2013.01.038).
- 510 Cordero-Grande, L., Christiaens, D., Hutter, J., Price, A.N., Hajnal, J.V.,  
511 2019. Complex diffusion-weighted image estimation via matrix recovery  
512 under general noise models. NeuroImage 200, 391–404. doi:[10.1016/j.neuroimage.2019.06.039](https://doi.org/10.1016/j.neuroimage.2019.06.039).
- 514 Dai, E., Ma, X., Zhang, Z., Yuan, C., Guo, H., 2017. Simultaneous multislice  
515 accelerated interleaved EPI DWI using generalized blipped-CAIPI acqui-  
516 sition and 3D K-space reconstruction. Magn. Reson. Med. 77, 1593–1605.  
517 doi:[10.1002/mrm.26249](https://doi.org/10.1002/mrm.26249).
- 518 Dai, E., Mani, M., McNab, J.A., 2023. Multi-band multi-shot diffu-  
519 sion MRI reconstruction with joint usage of structured low-rank con-  
520 straints and explicit phase mapping. Magn. Reson. Med. 89, 95–111.  
521 doi:[10.1002/mrm.29422](https://doi.org/10.1002/mrm.29422).

- 522 Dai, E., Zhang, Z., Ma, X., Dong, Z., Li, X., Xiong, Y., Yuan, C., Guo, H.,  
523 2018. The effects of navigator distortion and noise level on interleaved EPI  
524 DWI reconstruction: a comparison between image- and *k*-space method.  
525 Magn. Reson. Med. 80, 2024–2032. doi:[10.1002/mrm.27190](https://doi.org/10.1002/mrm.27190).
- 526 Dong, Z., Dai, E., Wang, F., Zhang, Z., Ma, X., Yuan, C., Guo, H., 2018.  
527 Model-based reconstruction for simultaneous multislice and parallel imag-  
528 ing accelerated multishot diffusion tensor imaging. Med. Phys. 45, 3196–  
529 3204. doi:[10.1002/mp.12974](https://doi.org/10.1002/mp.12974).
- 530 Garyfallidis, E., Brett, M., Amirbekian, B., Rokem, A., van der Walt, S.,  
531 Descoteaux, M., Nimmo-Smith, I., Contributors, D., 2014. DIPY, a library  
532 for the analysis of diffusion MRI data. Front. Neuroinform. 8, 1–17. doi:[10.3389/fninf.2014.00008](https://doi.org/10.3389/fninf.2014.00008).
- 533
- 534 Grissom, W.A., Sacolick, L., Vogel, M.W., 2010. Improving high-field MRI  
535 using parallel excitation. Imaging Med. 2, 675–693. doi:[10.2217/IIM.10.62](https://doi.org/10.2217/IIM.10.62).
- 536
- 537 Griswold, M.A., Jakob, P.M., Heidemann, R.M., Nittka, M., Jellus, V.,  
538 Wang, J., Kiefer, B., Haase, A., 2002. Generalized autocalibrating par-  
539 tially parallel acquisitions (GRAPPA). Magn. Reson. Med. 47, 1202–1210.  
540 doi:[10.1002/mrm.10171](https://doi.org/10.1002/mrm.10171).
- 541 Guhaniyogi, S., Chu, M.L., Chang, H.C., Song, A.W., Chen, N.K., 2016. Mo-  
542 tion immune diffusion imaging using augmented MUSE for high-resolution  
543 multi-shot EPI. Magn. Reson. Med. 75, 639–652. doi:[10.1002/mrm.25624](https://doi.org/10.1002/mrm.25624).

- 544 Hammernik, K., Klatzer, T., Kobler, E., Recht, M.P., Sodickson, D.K., Pock,  
545 T., Knoll, F., 2018. Learning a variational network for reconstruction of  
546 accelerated MRI data. *Magn. Reson. Med.* 79, 3055–3071. doi:[10.1002/mrm.26977](https://doi.org/10.1002/mrm.26977).
- 548 Heidemann, R.M., Porter, D.A., Anwander, A., Feiweier, T., Heberlein, K.,  
549 Knösche, T.R., Turner, R., 2010. Diffusion imaging in humans at 7 T  
550 using readout-segmented EPI and GRAPPA. *Magn. Reson. Med.* 64, 9–  
551 14. doi:[10.1002/mrm.22480](https://doi.org/10.1002/mrm.22480).
- 552 Hestenes, M.R., Stiefel, E., 1952. Methods of conjugate gradients for solving  
553 linear systems. *J. Res. Natl. Bur. Stand.* 49, 409–436. doi:[10.6028/jres.049.044](https://doi.org/10.6028/jres.049.044).
- 555 Hu, Y., Wang, X., Tian, Q., Yang, G., Daniel, B., McNab, J., Hargreaves, B.,  
556 2020. Multi-shot diffusion-weighted MRI reconstruction with magnitude-  
557 based spatial-angular locally low-rank regularization (SPA-LLR). *Magn.*  
558 *Reson. Med.* 83, 1596–1607. doi:[10.1002/mrm.28025](https://doi.org/10.1002/mrm.28025).
- 559 Huang, F., Vijayakumar, S., Li, Y., Hertel, S., Duensing, G.R., 2008. A soft-  
560 ware channel compression technique for faster reconstruction with many  
561 channels. *Magn. Reson. Imaging* 26, 133–141. doi:[10.1016/j.mri.2007.04.010](https://doi.org/10.1016/j.mri.2007.04.010).
- 563 Jeong, H.K., Gore, J.C., Anderson, A.W., 2013. High-resolution human  
564 diffusion tensor imaging using 2-D navigated multishot SENSE EPI at 7  
565 T. *Magn. Reson. Med.* 69, 793–802. doi:[10.1002/mrm.24320](https://doi.org/10.1002/mrm.24320).

- 566 Jones, D.K., 2010. Diffusion MRI: Theory, methods, and applications. Oxford  
567 University Press. doi:[10.1093/med/9780195369779.001.0001](https://doi.org/10.1093/med/9780195369779.001.0001).
- 568 Katscher, U., Börnert, P., Leussler, C., van den Brink, J.S., 2003. Transmit  
569 SENSE. Magn. Reson. Med. 49, 144–150. doi:[10.1002/mrm.10353](https://doi.org/10.1002/mrm.10353).
- 570 Knoll, F., Raya, J.G., Halloran, R.O., Baete, S., Sigmund, E., Bammer, R.,  
571 Block, T., Otazo, R., Sodickson, D.K., 2015. A model-based reconstruction  
572 for undersampled radial spin-echo DTI with variational penalties on the  
573 diffusion tensor. NMR Biomed 28, 353–366. doi:[10.1002/nbm.3258](https://doi.org/10.1002/nbm.3258).
- 574 Lam, F., Li, Y., Peng, X., 2019. Constrained magnetic resonance spectro-  
575 scopic imaging by learning nonlinear low-dimensional models. IEEE Trans.  
576 Med. Imaging 39, 545–555. doi:[10.1109/TMI.2019.2930586](https://doi.org/10.1109/TMI.2019.2930586).
- 577 Le Bihan, D., Breton, E., Lallemand, D., Grenier, P., Cabanis, E., Laval-  
578 Jeantet, M., 1986. MR imaging of intravoxel incoherent motions: appli-  
579 cation to diffusion and perfusion in neurologic disorders. Radiology 161,  
580 401–407. doi:[10.1148/radiology.161.2.3763909](https://doi.org/10.1148/radiology.161.2.3763909).
- 581 Liang, Z.P., 2007. Spatiotemporal imaging with partially separable functions,  
582 in: 2007 4th IEEE International Symposium on Biomedical Imaging: From  
583 Nano to Macro, pp. 988–991. doi:[10.1109/ISBI.2007.357020](https://doi.org/10.1109/ISBI.2007.357020).
- 584 Liu, C., Moseley, M.E., Bammer, R., 2005. Simultaneous phase cor-  
585 rection and SENSE reconstruction for navigated multi-shot DWI with  
586 non-Cartesian  $k$ -space sampling. Magn. Reson. Med. 54, 1412–1422.  
587 doi:[10.1002/mrm.20706](https://doi.org/10.1002/mrm.20706).

- 588 Lustig, M., Donoho, D., Pauly, J.M., 2007. Sparse MRI: The application of  
589 compressed sensing for rapid MR imaging. Magn. Reson. Med. 58, 1182–  
590 1195. doi:[10.1002/mrm.21391](https://doi.org/10.1002/mrm.21391).
- 591 Mani, M., Jacob, M., Kelley, D., Magnotta, V., 2017. Multi-shot sensitivity-  
592 encoded diffusion data recovery using structured low-rank matrix comple-  
593 tion (MUSSELS). Magn. Reson. Med. 78, 494–507. doi:[10.1002/mrm.26382](https://doi.org/10.1002/mrm.26382).
- 595 Mani, M., Magnotta, V.A., Jacob, M., 2021. qModeL: A plug-and-play  
596 model-based reconstruction for highly accelerated multi-shot diffusion MRI  
597 using learned priors. Magn. Reson. Med. 86, 835–851. doi:[10.1002/mrm.28756](https://doi.org/10.1002/mrm.28756).
- 599 Mansfield, P., 1977. Multi-planar image formation using NMR spin echoes.  
600 J Phys C 10, 55–58. doi:[10.1088/0022-3719/10/3/004](https://doi.org/10.1088/0022-3719/10/3/004).
- 601 Maudsley, A.A., 1980. Multiple-line-scanning spin density imaging. J. Magn.  
602 Reson. 41, 112–126. doi:[10.1016/0022-2364\(80\)90207-3](https://doi.org/10.1016/0022-2364(80)90207-3).
- 603 Merboldt, K.D., Hanicke, W., Frahm, J., 1985. Self-diffusion NMR imag-  
604 ing using stimulated echoes. J. Magn. Reson. 64, 479–486. doi:[10.1016/0022-2364\(85\)90111-8](https://doi.org/10.1016/0022-2364(85)90111-8).
- 606 Moeller, S., Pisharady, P.K., Ramanna, S., Lenglet, C., Wu, X., Dowdle,  
607 L., Yacoub, E., Uğurbil, K., Akçakaya, M., 2021. NOise reduction with  
608 DIistribution Corrected (NORDIC) PCA in dMRI with complex-valued  
609 parameter-free locally low-rank processing. NeuroImage 226, 117539.  
610 doi:[10.1016/j.neuroimage.2020.117539](https://doi.org/10.1016/j.neuroimage.2020.117539).

- 611 Mori, S., Crain, B.J., Chacko, V.P., Van Zijl, P.C.M., 1999. Three-  
612 dimensional tracking of axonal projections in the brain by mag-  
613 netic resonance imaging. Ann. Neurol. 45, 265–269. doi:[10.1002/1531-8249\(199902\)45:2<265::AID-ANA21>3.0.CO;2-3](https://doi.org/10.1002/1531-8249(199902)45:2<265::AID-ANA21>3.0.CO;2-3).
- 614
- 615 Ong, F., Lustig, M., 2019. SigPy: A Python package for high performance  
616 iterative reconstruction, in: Proceedings of the 27th Annual Meeting of  
617 ISMRM, Montréal, CAN, p. 4819. doi:[10.5281/zenodo.5893788](https://doi.org/10.5281/zenodo.5893788).
- 618 Ong, F., Zhu, X., Cheng, J.Y., Johnson, K.M., Larson, P.E.Z., Vasanawala,  
619 S.S., Lustig, M., 2020. Extreme MRI: Large-scale volumetric dynamic  
620 imaging from continuous non-gated acquisitions. Magn. Reson. Med. 84,  
621 1763–1780. doi:[10.1002/mrm.28235](https://doi.org/10.1002/mrm.28235).
- 622 Pipe, J.G., Farthing, V.G., Forbes, K.P., 2002. Multishot diffusion-weighted  
623 FSE using PROPELLER MRI. Magn. Reson. Med. 47, 42–52. doi:[10.1002/mrm.10014](https://doi.org/10.1002/mrm.10014).
- 624
- 625 Polak, D., Splitthoff, D.N., Clifford, B., Lo, W.C., Huang, S.Y., Conklin, J.,  
626 Wald, L.L., Setsompop, K., Cauley, S., 2022. Scout accelerated motion  
627 estimation and reduction (SAMER). Magn. Reson. Med. 87, 163–178.  
628 doi:[10.1002/mrm.28971](https://doi.org/10.1002/mrm.28971).
- 629 Porter, D.A., Heidemann, R.M., 2009. High resolution diffusion-weighted  
630 imaging using readout-segmented echo-planar imaging, parallel imaging  
631 and a two-dimensional navigator-based reacquisition. Magn. Reson. Med.  
632 62, 468–475. doi:[10.1002/mrm.22024](https://doi.org/10.1002/mrm.22024).

- 633 Pruessmann, K.P., Weiger, M., Scheidegger, M.B., Boesiger, P., 1999.  
634 SENSE: Sensitivity encoding for fast MRI. Magn. Reson. Med. 42, 952–  
635 962. doi:[10.1002/\(SICI\)1522-2594\(199911\)42:5<952::AID-MRM16>3.0.CO;2-S](https://doi.org/10.1002/(SICI)1522-2594(199911)42:5<952::AID-MRM16>3.0.CO;2-S).
- 637 Ra, J.B., Rim, C.Y., 1993. Fast imaging using subencoding data sets from  
638 multiple detectors. Magn. Reson. Med. 30, 142–145. doi:[10.1002/mrm.1910300123](https://doi.org/10.1002/mrm.1910300123).
- 640 Roemer, P.B., Edelstein, W.A., Hayes, C.E., Souza, S.P., Mueller, O.M.,  
641 1990. The NMR phased array. Magn. Reson. Med. 16, 192–225. doi:[10.1002/mrm.1910160203](https://doi.org/10.1002/mrm.1910160203).
- 643 Setsompop, K., Fan, Q., Stockmann, J., Bilgic, B., Huang, S., Cauley, S.F.,  
644 Nummenmaa, A., Wang, F., Rathi, Y., Witzel, T., Wald, L.L., 2018. High-  
645 resolution *in vivo* diffusion imaging of the human brain with generalized  
646 slice dithered enhanced resolution: Simultaneous multislice (gSlider-SMS).  
647 Magn. Reson. Med. 79, 141–151. doi:[10.1002/mrm.26653](https://doi.org/10.1002/mrm.26653).
- 648 Setsompop, K., Gagoski, B.A., Polimeni, J.R., Witzel, T., Wedeen, V.J.,  
649 Wald, L.L., 2012. Blipped-controlled aliasing in parallel imaging for si-  
650 multaneous multislice echo planar imaging with reduced *g*-factor penalty.  
651 Magn. Reson. Med. 67, 1210–1224. doi:[10.1002/mrm.23097](https://doi.org/10.1002/mrm.23097).
- 652 Shafieizargar, B., Jeurissen, B., Poot, D.H.J., Klein, S., Van Audekerke,  
653 J., Verhoye, M., den Dekker, A.J., Sijbers, J., 2023. ADEPT: Accurate  
654 diffusion echo-planar imaging with multi-contrast shTs. Magn. Reson.  
655 Med. 89, 396–410. doi:[10.1002/mrm.29398](https://doi.org/10.1002/mrm.29398).

- 656 Tournier, J.D., Smith, R., Raffelt, D., Tabbara, R., Dhollander, T., Pietsch,  
657 M., Christiaens, D., Jeurissen, B., Yeh, C.H., Connelly, A., 2019. MRtrix3:  
658 A fast, flexible and open software framework for medical image processing  
659 and visualisation. NeuroImage 202, 116137. doi:<https://doi.org/10.1016/j.neuroimage.2019.116137>.
- 661 Trzasko, J., Manduca, A., 2011. Local versus global low-rank promotion in  
662 dynamic MRI series reconstruction, in: Proceedings of the 19th Annual  
663 Meeting of ISMRM, Montréal, CAN, p. 4371.
- 664 Tuch, D.S., Reese, T.G., Wiegell, M.R., Makris, N., Belliveau, J.W., Wedeen,  
665 V.J., 2002. High angular resolution diffusion imaging reveals intravoxel  
666 white matter fiber heterogeneity. Magn. Reson. Med. 48, 577–582. doi:[10.1002/mrm.10268](https://doi.org/10.1002/mrm.10268).
- 668 Uecker, M., Lai, P., Murphy, M.J., Virtue, P., Elad, M., Pauly, J.M.,  
669 Vasanawala, S.S., Lustig, M., 2014. ESPIRiT – an eigenvalue approach  
670 to autocalibrating parallel MRI: Where SENSE meets GRAPPA. Magn.  
671 Reson. Med. 71, 990–1001. doi:[10.1002/mrm.24751](https://doi.org/10.1002/mrm.24751).
- 672 Wu, W., Koopmans, P.J., Andersson, J.L., Miller, K.L., 2019. Diffusion  
673 Acceleration with Gaussian process Estimated Reconstruction (DAGER).  
674 Magn. Reson. Med. 82, 107–125. doi:[10.1002/mrm.27699](https://doi.org/10.1002/mrm.27699).
- 675 Wu, W., Miller, K.L., 2017. Image formation in diffusion MRI: A review  
676 of recent technical developments. J. Magn. Reson. Imaging 46, 646–662.  
677 doi:[10.1002/jmri.25664](https://doi.org/10.1002/jmri.25664).

678 Zhang, T., Pauly, J.M., Levesque, I.R., 2015. Accelerated parameter mapping  
679 with a locally low rank constraint. Magn. Reson. Med. 73, 655–661. doi:[10.1002/mrm.25161](#).  
680